Atomistic mechanisms governing elastic limit and incipient plasticity in crystals

Ju Li*†, Krystyn J. Van Vliet†‡, Ting Zhu*, Sidney Yip*‡ & Subra Suresh‡

** Department of Nuclear Engineering, ‡ Department of Materials Science and Engineering, Massachusetts Institute of Technology, 77 Massachusetts Avenue, Cambridge, Massachusetts 02139, USA*
† These authors contributed equally to this work

Nanometre-scale contact experiments[1–6] and simulations[7–10] demonstrate the potential to probe incipient plasticity—the onset of permanent deformation—in crystals. Such studies also point to the need for an understanding of the mechanisms governing defect nucleation in a broad range of fields and applications. Here we present a fundamental framework for describing incipient plasticity that combines results of atomistic and finite-element modelling, theoretical concepts of structural stability at finite strain, and experimental analysis. We quantify two key features of the nucleation and subsequent evolution of defects. A position-sensitive criterion based on elastic stability determines the location and character of homogeneously nucleated defects. We validate this stability criterion at both the atomistic and the continuum levels. We then propose a detailed interpretation of the experimentally observed sequence of displacement bursts to elucidate the role of secondary defect sources operating locally at stress levels considerably smaller than the ideal strength required for homogeneous nucleation. These findings provide a self-consistent explanation of the discontinuous elastic–plastic response in nanoindentation measurements, and a guide to fundamental studies across many disciplines that seek to quantify and predict the initiation and early stages of plasticity.

Characteristic discontinuities have been observed consistently in the measured load–penetration depth (P–h) response of single crystals indented to nanometre-scale depths[1–5]. Before the first discontinuity, local shear stresses beneath the nominally sharp indenter approach the theoretical strength of the indented crystal, indicating that homogeneous defect nucleation is a logical starting event for subsequent incipient (that is, early-stage) plasticity (Fig. 1a). This hypothesis is supported by recent *in situ* experiments[6] using the Bragg–Nye bubble raft analogue, showing that nanoindentation of a two-dimensional (2D) crystal indeed results in homogeneous dislocation nucleation. However, the present level of quantitative understanding of the mechanisms by which contact-induced plasticity initiates and evolves in three-dimensional (3D) crystals is still limited.

The displacement bursts in the load-controlled experiment of Fig. 1a would appear as sharp decreases in load (dips) in a displacement-controlled experiment, as shown for a simulated displacement-controlled response in Fig. 1b. These dips correspond to elastic instabilities that can be predicted by a free-energy-based, position-dependent criterion, and its validity demonstrated at both the atomic and continuum levels. To show this, we consider a representative volume element V subjected to homogeneous deformation at finite strain to a current configuration $\mathbf{x}$. Expanding the free energy F to the second order in incremental displacement $\mathbf{u}(\mathbf{x})$, we obtain (J.L. *et al.*, manuscript in preparation)

$$\Delta F = \frac{1}{2}\int_{V(\mathbf{x})} D_{ijkl}u_{i,j}(\mathbf{x})u_{k,l}(\mathbf{x})\,\mathrm{d}V \qquad (1)$$

where $D_{ijkl} \equiv C_{ijkl} + \tau_{jl}\delta_{ik}$, C is the elastic constants tensor, τ is the internal or Cauchy stress tensor, and $u_{i,j} \equiv \partial u_i(\mathbf{x})/\partial x_j$. Substitution of a plane wave perturbation, $u_i(\mathbf{x}) = w_i \exp(i\mathbf{k}\cdot\mathbf{x})$, into equation (1) leads to the following stability condition for the representative volume element:

$$\Lambda(\mathbf{w},\mathbf{k}) \equiv (C_{ijkl}w_i w_k + \tau_{jl})k_j k_l > 0 \qquad (2)$$

The sign of $\Lambda(\mathbf{w}, \mathbf{k})$ reflects the concavity of F ($\mathbf{w}$ is the polarization vector, and $\mathbf{k}$ the wavevector). If there exists a pair of $\mathbf{w}$, $\mathbf{k}$ such that $\Lambda(\mathbf{w}, \mathbf{k})$ is negative, then homogeneity of this representative volume element cannot be maintained and defect singularities will form internally in four stages. (1) Linear growth of the unstable elastic wave, well-described by continuum; (2) nonlinear evolution at larger amplitudes, over which the wave profile steepens; (3) progressive steepening of the wave front until its width approaches atomic spacing, upon which its description must be transferred from a continuum to an atomistic basis; and (4) arrest of the atomistically sharp wave front in a low-dimensional atomic

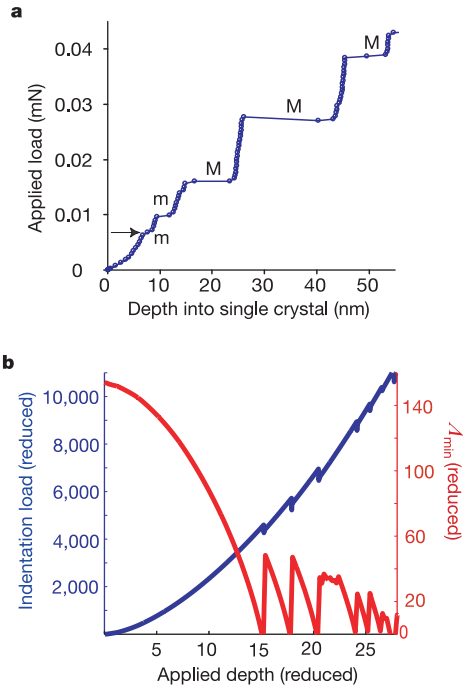

Figure 1 Nanoindentation responses. **a**, Experimentally measured applied load–displacement response of {111} single-crystal aluminium[4] showing an initial displacement burst (arrow). Following this first event, multiple displacement bursts can be observed. The displacement bursts are either minor (m), spanning ~2 nm or less, or major (M), 10 nm or more, both at essentially constant applied load. A minor burst indicates a single slip event whereby just one prismatic or glide loop is created, which then propagates until being stopped at the substrate (or at a grain boundary in the case of a polycrystal). In contrast, a major burst indicates at least ten consecutive complete slips, at no observable increase in applied load. Just one such major burst would exhaust at least a significant portion of the elastic energy stored in a particular slip system[4]. **b**, Applied displacement–load response (blue) of MD simulated bubble raft, showing correlation of load drops with a sequence of observed homogeneous dislocation dipole nucleation events. The elastic instability criterion $\Lambda_{\min}$ (red) tends to zero for the first several nucleation events. All nucleation events occur subsurface; the high mobility of the dissociated dipoles immediately restores the region beneath the indenter to crystallize order after nucleation. Our interbubble potential is of the form $V(r) = \alpha(r-1)^4 - \beta(r-1)^2$, where r is the interbubble distance. Length and energy units represented by the cut-off radius and potential well-depth, respectively, are set equal to unity such that the potential well shape is controlled by a single parameter, the equilibrium distance r_0, set equal to 0.85. The indenter of radius $R = 160$ is implemented as a frictionless, external potential on the bubbles. The bubble raft is 340 × 212 in dimension, containing 115,200 bubbles for this in-plane orientation.

© 2002 Nature Publishing Group

energy profile, at which point a defect is nucleated. If the wave is transverse, the instability will probably result in the formation of a dislocation or twin of slip plane normal $\mathbf{k}$ and Burgers vector orientation $\mathbf{w}$; if the wave is longitudinal, a microcrack would result. The elastic stability of the representative volume element thus can be determined by minimizing $\Lambda(\mathbf{w},\mathbf{k})$ with respect to the polarization vector $\mathbf{w}$ and wavevector $\mathbf{k}$, $\Lambda_{\min} \equiv \min_{|\mathbf{w}|=1,|\mathbf{k}|=1}\Lambda(\mathbf{w},\mathbf{k})$. By interpreting $\Lambda_{\min}$ as a measure of microstiffness that varies locally, instability is predicted at the position where $\Lambda_{\min}$ vanishes. Note that equation (2) is an energy-based criterion; its minimization at a material point is, in fact, environment-dependent. The present approach is different from the analysis of instability under homogeneous loading[11–13] in two respects. In the case of nanoindentation, stress applied via the frictionless indenter is nonuniform and thus can create an elastically unstable volume that is isolated physically from the external loading. Secondly, our derivation is the first (to our knowledge) such expression capable of predicting not only the location of elastic instability, but also the slip character (slip plane and Burgers vector) of the corresponding defect, as shown below.

As a criterion derived from the free energy, equation (2) is equivalent to the continuum-based condition discussed formally by Hill[14] in the context of acceleration waves and by Rice[15] when considering shear band formation. In our implementation we ascribe to each atom an atomistic stress tensor[16] and an elastic constant tensor[17], and identify the 'softest atom' by minimizing $\Lambda(\mathbf{w},\mathbf{k})$ for each atom iteratively, first with respect to $\mathbf{w}$ and then with respect to $\mathbf{k}$ to obtain a self-consistent $\Lambda_{\min}$. The lowest $\Lambda_{\min}$ found at a given indenter displacement is shown for a 2D, molecular dynamics (MD) simulation of the Bragg–Nye raft (Fig. 1b). During elastic deformation, $\Lambda_{\min}$ decreases monotonically and vanishes exactly when the first load dip occurs. The correspondence between a load dip and the vanishing of $\Lambda_{\min}$ continues for five subsequent dips. Furthermore, we find that the $\mathbf{w}$ and $\mathbf{k}$ vectors that minimize $\Lambda(\mathbf{w},\mathbf{k})$ agree well with the slip direction and slip plane normal, respectively, observed in MD simulations, which are also consistent with the primary slip system of the face-centred cubic crystallographic lattice. Considering the complexity of the numerical evaluations, we regard the results of Fig. 1b as significant and quantitative validation of the stability criterion in both formulation and implementation. To our knowledge, this is the first demonstration of a site-specific stability criterion at the atomic scale.

We have extended this stability analysis to finite element calculations based on Cauchy–Born elasticity[18] by incorporating large strain constitutive relations provided directly by interatomic potentials. In contrast to the quasicontinuum method developed by Tadmor *et al.*[19], which in principle should give the same result for the present nucleation problem, our approach remains a fully continuum method that is capable of describing the elastic instabilities predicted by the Λ-criterion. Its implementation in a standard finite element software package[20] requires only that the user supply the exact Cauchy–Born constitutive relation, which comes directly from a static (temperature $T = 0$) or ensemble-averaged lattice sum calculating at every step with the appropriate interatomic potential. This method allows us to identify the lowest $\Lambda_{\min}$ among all nodes,

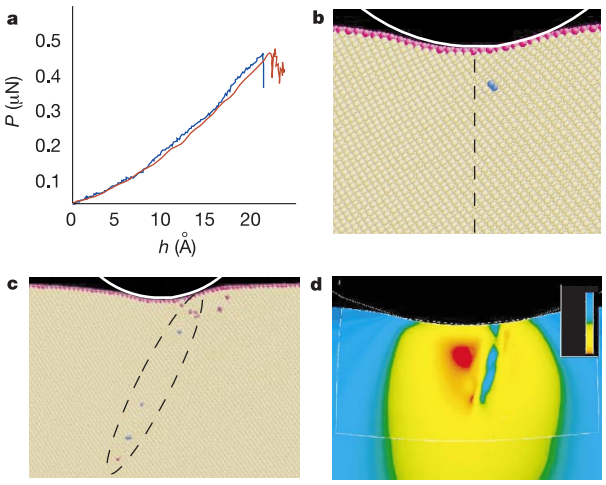

Figure 2 Correspondence of MD and FEM simulations in ⟨111⟩ cylindrical indentation of Cu. In both simulations, the long axis of the cylinder is along ⟨110⟩. **a**, Applied displacement–load responses (h–P) showing correlation of load relaxation with homogeneous defect nucleation. The FEM response (blue) shows good agreement with MD (red) for the initial, elastic loading response and the critical load required to nucleate a defect. **b**, MD simulation comprising 290,304 atoms and periodic boundary conditions, showing that the nucleation site (blue) is off the centre axis (dashed line) by ~20%, and at a depth ~60% of the contact radius a. Indenter radius $R = 20$ nm. Atoms are colour-encoded by coordination number N: yellow, $N = 12$; blue, $N \neq 12$. The lack of left–right symmetry and decreased depth of nucleation are due to the elastic anisotropy of Cu, and are consistent with the recently developed linear elastic, anisotropic solution for a cylindrical punch[23]. **c**, MD simulation after several dipole nucleation events illustrating the formation of a shear band (dashed lines) after the dissociation of dislocation pairs to the free surface and crystalline interior. **d**, FEM simulation of the initial defect nucleation event (elements are colour-encoded by the Mises stress, red and blue denote maximum and minimum values respectively) showing that shear localization spontaneously appears immediately after $\Lambda_{\min} = 0$. The predicted nucleation site, slip plane normal and Burgers vector all agree with MD observations after the event.

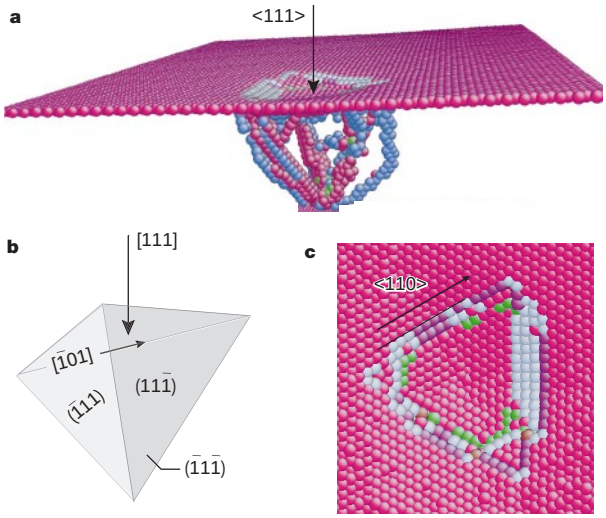

Figure 3 Homogeneous defect nucleation in ⟨111⟩ spherical indentation of Al. **a**, MD simulation of spherical indentation ($R = 12$ nm) normal to the ⟨111⟩ surface of Al results in a sessile structure derived from homogeneously nucleated glide loops on three equivalent {111} planes. The simulation comprises 326,592 atoms and periodic boundary conditions, using the Ercolessi potential[24] for Al. Atom colour indicates coordination number N: light pink, surface coordination, $N = 9$; atoms with perfect coordination $N = 12$ are made invisible. Other colours (green, blue and light pink interior atoms) indicate under- or over-coordinated atoms, which are atoms comprising defects. **b**, Diagram of the {111}⟨110⟩ slip systems available for indentation in the ⟨111⟩ direction. Symmetric arrangement of the systems indicates that homogeneous nucleation of dislocation loops on multiple slip systems must result in loop intersection and, consequently, sessile dislocation segments in the interior of the crystal. **c**, Top view of the MD simulation surface showing the ⟨110⟩ orientations of three slip steps (surface ledges) that result from the initial nucleation event. The surface ledge corners then act as stress concentrators for further heterogeneous nucleation events.

© 2002 Nature Publishing Group

thereby predicting homogeneous defect nucleation in accordance with an atomic-scale strain-to-failure criterion. Direct comparison of the load–displacement responses for cylindrical ⟨111⟩ indentation of Cu obtained by direct MD and the aforementioned finite element method (FEM) using the same interatomic potential[21] is shown in Fig. 2a. The close correspondence in the elastic loading and the critical load for defect nucleation given by these two traditionally different methods of modelling is noteworthy. Further validation of our interatomic-potential-based FEM calculation against direct MD under the condition of large nonlinear strain and homogeneous defect nucleation is demonstrated by the fidelity of the nucleation site, slip plane, and Burgers vector obtained from these two approaches (Fig. 2b–d).

We next consider MD simulations of spherical indentation, showing the atomic-level details of dislocation nucleation and subsequent incipient plasticity. Figure 3a shows that defect nucleation during displacement-controlled ⟨111⟩ nanoindentation of Al occurs near the surface as expanding glide loops on three equivalent {111}⟨110⟩ slip systems (Fig. 3b). Kelchner *et al.* reported initial glide loop nucleation for atomistic simulations of spherical ⟨111⟩ indentation in another face-centred cubic crystal (Au), but did not observe the three-fold symmetry of the defect structure[7]. This contrast may be due to differences in elastic anisotropy of the crystal, stacking fault energy, and the computational method employed (Kelchner *et al.* used energy minimization, as opposed to MD). Owing to the inward orientation of the {111} planes activated during indentation of Al, the glide loops expand and intersect to produce three, intersecting ⟨110⟩-oriented slip steps on the surface (Fig. 3c). Upon increasing indenter displacement, loops nucleate on adjacent {111} planes; four such loops interact, with a segment from each forming one side of a parallelogram (Fig. 4a). This prismatic loop structure moves through the crystal along its glide prism to the bottom of the substrate (Fig. 4b and Supplementary Information Fig. 1). It is important to note that the prismatic loops are not homogeneously nucleated; instead they are emitted near the surface, aided by the reaction products of homogeneously nucleated glide loops. As shown in 3D simulations for Cu (Supplementary Information Fig. 2), increased elastic anisotropy alters the lock/source formation in ⟨111⟩ indentation, leading to an incipient plasticity mode more similar to 2D observations, that is, expansion of glide loops and twinning.

We now analyse the experimental observations of {111} single-crystal Al (ref. 4), indented with a nominally sharp indenter (approximate indenter tip radius $R = 50$ nm), as shown in Fig. 1a. The P–h response is elastic until a shear stress of ~5.5 GPa is attained beneath the rounded tip. If both the initial and subsequent slip events were homogeneously nucleated, then each subsequent event would require gigapascal-level local stresses observed as an increase in applied load (hardening). Experimentally, however, no apparent hardening is observed during major displacement bursts, which correspond to the creation and propagation of ~50 complete slip events[4]. Thus, a hypothesis of multiple homogeneously nucleated prismatic loops is incompatible with the experimental data on major bursts. With reference to our MD simulations, we suggest that incipient plasticity is initiated by homogeneously nucleated glide loops that subsequently react to form 3D, secondary dislocation sources similar to the Frank–Read source. These sources operate at megapascal-level local stresses until most of the stored elastic energy is exhausted. After significant emission from a single secondary source, back-stresses from dislocation pile-up counteract the external resolved stress for the corresponding slip system, thereby shutting down this dislocation source. Subsequent bursts occur only when the applied load is increased sufficiently to cause existing sources to emit single dislocation loops discretely, resulting in minor relaxations. The minor bursts and hardening continue until the creation of a source on a different slip system, leading to a second major relaxation, and this process repeats. This interpretation, supported by recent atomistic calculations which show that inhomogeneities such as atomic steps and grooves near the indented surface can greatly reduce the nucleation stress in nanoindentation[8,22], provides a self-consistent, mechanism-based explanation of the observed transition from the onset of elastic instability to incipient plasticity in nanoindentation responses such as Fig. 1a.

Although our study is framed in the context of indentation, the quantitative and predictive capabilities of our results have implications for both experimental and computational investigations of large-strain deformation phenomena. For example, dislocation

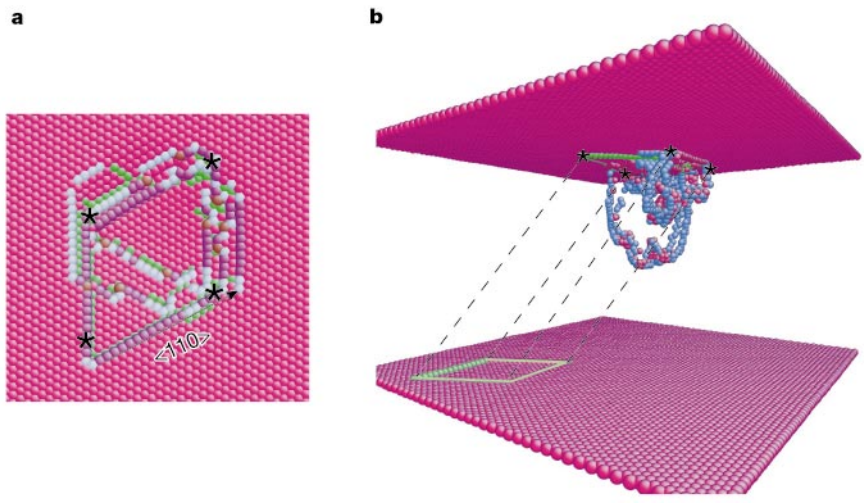

Figure 4 Incipient plasticity in ⟨111⟩ spherical indentation of Al. **a**, Plan view of the MD simulation comprising 350,000 atoms. The intersection points (stars) indicate the corners of the emitted prismatic loop. **b**, On further indenter displacement, dislocation half-loops on two {111}⟨110⟩ slip systems cross-slip and pinch off from the surface, forming a prismatic dislocation loop which moves through the crystal along its glide prism (dashed lines) without increasing in loop diameter. Atom colour corresponds to coordination number N as described in Fig. 3 legend. A parallelogram slip mark is left on the bottom surface when the prismatic loop leaves the lower, unconstrained film surface.

© 2002 Nature Publishing Group

dynamics studies of strain hardening that at present assume an initial dislocation configuration could incorporate the proposed interatomic-potential-based FEM to solve for the regular stress field solution component, and use the Λ-criterion to nucleate new, embryonic dislocation loops. Likewise, experimental studies of the initiation and early stages of nanoscale deformation via slip, twinning or cracking could be designed to exploit the above-mentioned effects of crystallographic orientation, elastic anisotropy and boundary conditions. □

Received 25 February; accepted 22 May 2002; doi:10.1038/nature00865.

1. Gerberich, W. W., Venkataraman, S. K., Huang, H., Harvey, S. E. & Kohlstedt, D. L. The injection of plasticity by millinewton contacts. *Acta Metal. Mater.* **43,** 1569–1576 (1995).
2. Suresh, S., Nieh, T.-G. & Choi, B. W. Nanoindentation of copper thin films on silicon substrates. *Scripta Mater.* **41,** 951–957 (1999).
3. Kiely, J. D., Jarausch, K. F., Houston, J. E. & Russell, P. E. Initial stages of yield in nanoindentation. *J. Mater. Res.* **15,** 4513–4519 (1999).
4. Gouldstone, A., Koh, H.-J., Zeng, K. Y., Giannakopoulos, A. E. & Suresh, S. Discrete and continuous deformation during nanoindentation of thin films. *Acta Mater.* **48,** 2277–2295 (2000).
5. Kramer, D. E., Yoder, K. B. & Gerberich, W. W. Surface constrained plasticity: Oxide rupture and the yield point process. *Phil. Mag. A* **81,** 2033–2058 (2001).
6. Gouldstone, A., Van Vliet, K. J. & Suresh, S. Nanoindentation: Simulation of defect nucleation in a crystal. *Nature* **411,** 656 (2001).
7. Kelchner, C. L., Plimpton, S. J. & Hamilton, J. C. Dislocation nucleation and defect structure during surface indentation. *Phys. Rev. B* **58,** 11085–11088 (1998).
8. Zimmerman, J. A., Kelchner, C. L., Klein, P. A., Hamilton, J. C. & Foiles, S. M. Surface step effects on nanoindentation. *Phys. Rev. Lett.* **87,** 165507 (2001).
9. Tadmor, E. B., Miller, R. & Phillips, R. Nanoindentation and incipient plasticity. *J. Mater. Res.* **14,** 2233–2250 (1999).
10. Shenoy, V. B., Phillips, R. & Tadmor, E. B. Nucleation of dislocations beneath a plane strain indenter. *J. Mech. Phys. Solids* **48,** 649–673 (2000).
11. Wang, J., Li, J., Yip, S., Phillpot, S. & Wolf, D. Mechanical instabilities of homogeneous crystals. *Phys. Rev. B* **52,** 12627–12635 (1995).
12. Zhou, Z. & Joos, B. Stability criteria for homogeneously stressed materials and the calculation of elastic constants. *Phys. Rev. B* **54,** 3841–3850 (1996).
13. Morris, J. W. & Krenn, C. R. The internal stability of an elastic solid. *Phil. Mag. A* **80,** 2827–2840 (2000).
14. Hill, R. Acceleration waves in solids. *J. Mech. Phys. Solids* **10,** 1–16 (1962).
15. Rice, J. R. in *Theoretical and Applied Mechanics* (ed. Koiter, W. T.) Vol. 1, 207–220 (North-Holland, Amsterdam, 1976).
16. Egami, T., Maeda, K. & Vitek, V. Structural defects in amorphous solids. A computer simulation study. *Phil. Mag. A* **41,** 883–901 (1980).
17. Ray, J. R. Elastic constants and statistical ensembles in molecular dynamics. *Comput. Phys. Rep.* **8,** 109–152 (1988).
18. Ericksen, J. L. in *Phase Transformations and Material Instabilities in Solids* (ed. Gurtin, M. E.) 61–78 (Academic, Orlando, 1984).
19. Tadmor, E. B., Ortiz, M. & Phillips, R. Quasicontinuum analysis of defects in solids. *Phil. Mag. A* **73,** 1529–1563 (1996).
20. *ABAQUS Theory Manual Version 6.1* (Hibbitt, Karlsson and Sorensen, Pawtucket, Rhode Island, 2000).
21. Ackland, G. J., Bacon, D. J., Calder, A. F. & Harry, T. Computer simulation of point defect properties in dilute Fe-Cu alloy using a many-body interatomic potential. *Phil. Mag. A* **75,** 713–732 (1997).
22. Brochard, S., Beauchamp, P. & Grilhe, J. Simulations of dislocation nucleation from atomic size surface steps and grooves. *Mater. Sci. Eng. A* **309–310,** 456–462 (2001).
23. Hwu, C. & Fan, C. W. Solving the punch problems by analogy with the interface crack problems. *Int. J. Solids Struct.* **35,** 3945–3960 (1998).
24. Ercolessi, F. & Adams, J. B. Interatomic potentials from first-principles calculations: the force-matching method. *Europhys. Lett.* **26,** 583–588 (1994).

Supplementary Information accompanies the paper on *Nature*'s website (http://www.nature.com/nature).

Acknowledgements

This work was supported by the Defense University Research Initiative on NanoTechnology (DURINT) on 'Damage- and Failure-Resistant Nanostructured and Interfacial Materials' which is supported at the Massachusetts Institute of Technology by the Office of Naval Research. We thank A. S. Argon for comments. K.J.V.V. acknowledges the National Defense Science and Engineering Graduate Fellowship programme. J.L., T.Z. and S.Y. acknowledge support by Honda R&D, AFOSR, NSF/KDI/DMR, and Lawrence Livermore National Laboratory.

Competing interests statement

The authors declare that they have no competing financial interests.

Correspondence and requests for materials should be addressed to S.Y. (e-mail: syip@mit.edu).

Dynamic fracture by large extraterrestrial impacts as the origin of shatter cones

Amir Sagy*, Ze'ev Reches* & Jay Fineberg†

** Institute of Earth Sciences, † The Racah Institute of Physics, The Hebrew University of Jerusalem, 91904 Jerusalem, Israel*

A large impact by a comet or meteorite releases an enormous amount of energy, which evaporates, melts and fractures the surrounding rocks[1–4]. Distinctive features of such impacts are 'shatter cones', deformed rocks characterized by hierarchical striated features[5,6]. Although such features have been used for decades as unequivocal fingerprints of large-body impacts, the process by which shatter cones form has remained enigmatic. Here we show that the distinctive shatter-cone striations naturally result from nonlinear waves (front waves) that propagate along a fracture front[7–10]. This explains the observed systematic increase of striation angles with the distance from the impact. Shatter-cone networks, typically spanning many scales, can be understood as hierarchical bifurcations of the fracture front, which is generated by the immense energy flux carried by the initial, impact-generated, shock waves. Our quantitative predictions based on this theory are supported by field measurements at the Kentland and Vredefort impact sites. These measurements indicate that shatter cones near to the impact site were formed by fractures propagating at nearly the Rayleigh wave speed of the host rocks, whereas the furthest shatter cones observed (about 40 km from the impact site) were formed by fronts moving more slowly. These results provide insight into impact dynamics as well as dissipative mechanisms in solids subjected to sudden, extremely intense fluxes of energy.

The formidable shock waves generated during large extraterrestrial impacts intensely deform crustal rock[1–4]. Beyond the near-impact region, where rock evaporation and melting prevail, shock-induced structures are dominant[3,11]. Some of the most distinct of these structures are shatter cones (Fig. 1a and b), which are observed in nature only at large impact sites. They range in size from a few centimetres to a few metres[5,11], and generally occur within hierarchic networks—called 'horse-tail' structures[5]—in which cascades of contiguous cones of monotonously decreasing size are observed (Fig. 1b). Although shatter cones are frequently semiconical, complete cones are rare[12,13], and, in many cases, their characteristic striations are observed on nearly planar surfaces[14] (Fig. 1b).

The precise mechanism for shatter-cone formation is unknown. It has been shown that conical shapes could result either from the interaction of shock waves with point inhomogeneities in rocks[15], or from interactions between the main compressive shock and rebound waves[16]. However, these models do not explain the dominant features of shatter cones: characteristic striations (Fig. 1a), the 'horse-tail' cone hierarchy (Fig. 1b), and the rarity of complete cones. Here we present a new model for shatter-cone formation that is based on recent developments in the study of dynamic fracturing[7–10]. This model explains the characteristic features of shatter cones, and its predictions are supported by field observations at the classic impact sites of Vredefort, South Africa, and Kentland, Indiana.

The Kentland impact deformed a thick sequence of Mesozoic carbonate and clastic rocks. A quarry, 1 km^2 in area and 200 m in depth, in the central, uplifted part of this impact provides large, three-dimensional shatter-cone exposures. Our fieldwork reveals that shatter cones are not separable, isolated objects within the rock mass, but are secondary structures that are generated along the

© 2002 Nature Publishing Group